PCCP

Accepted Manuscript




ROYAL SOCIETY OF CHEMISTRY

www.rsc.org/pccp

Journal Name

ARTICLE TYPE

Cite this: DOI: 10.1039/xxxxxxxxxx

# Laser induced alignment of state-selected $CH_3I$.

Lanhai He,[a,b] Jaap Bulthuis,[c] Sizuo Luo,[a,b] Jia Wang,[a,b] Chunjing Lu,[a,b] Steven Stolte,[a,b,c] Dajun Ding*[a,b] and Wim G. Roeterdink[a,b]

Received Date
Accepted Date

DOI: 10.1039/xxxxxxxxxx

www.rsc.org/journalname

Hexapole state selection is used to prepare $CH_3I$ molecules in the $|JKM\rangle = |1 \pm 1 \mp 1\rangle$ state. The molecules are aligned in a strong 800 nm laser field, which is linearly polarised perpendicular to the weak static extraction field E of the time of flight setup. The molecules are subsequently ionised by a second time delayed probe laser pulse. It will be shown that in this geometry at high enough laser intensities the Newton sphere has sufficient symmetry to apply the inverse Abel transformation to reconstruct the three dimensional distribution from the projected ion image. The laser induced controllable alignment was found to have the upper and lower extreme values of $\langle P_2(\cos\theta)\rangle$ = 0.7 for the aligned molecule and -0.1 for the anti-aligned molecule, coupled to a $\langle P_4(\cos\theta)\rangle$ between 0.3 and 0.0. The method to extract the alignment parameters $\langle P_2(\cos\theta)\rangle$ and $\langle P_4(\cos\theta)\rangle$ directly from the velocity map ion images will be discussed.

## 1 Introduction

Control over the molecular axis distribution is of importance in the fields of reaction dynamics and intense laser field physics. In chemical reaction dynamics the mutual orientation of the reactants plays a key role in the detailed reaction mechanism. The effect of orientation and alignment of the reactants on the reaction products has been the subject of many studies.[1–6] Strong field electron re-scattering phenomena occurring in Above Threshold ionisation (ATI), Non Sequential Double ionisation (NSDI) and High Harmonics Generation (HHG) are the result of the collision between the returning electron wavepacket and the ion.[7–10] The random orientation of the molecules in the molecular beam will lower the amount of information which can be extracted from these re-scattering experiments due to the inevitable averaging over the molecular orientation. Laser alignment of molecules gives direct access to information in the molecular frame and makes orbital tomography employing electron re-scattering possible.[11,12] Alignment of molecules with intense laser pulses has been demonstrated for cold molecules in a molecular beam expansion using laser pulses ranging from nanoseconds to femtoseconds.[13–19] In these experiments cold molecular beams are used, although still numerous rotational states are present which exhibit different degrees of alignment. Rotational state selection techniques can enhance the achievable maximum alignment. Nielsen *et al.* used an inhomogeneous electrostatic dipole field to select the J = 0 state of the OCS molecule before alignment. Holmegaard *et al.* and Filsinger *et al.* applied this technique to obtain a very high alignment of iodobenzene.[20–22] Ghafur *et al.* used the hexapole state selection technique in combination with pulse shaping techniques to achieve very high degrees of orientation in NO molecules.[23]

The symmetry axis of a polar symmetric top, with respect to the laser polarisation vector, can be written as an expansion in Legendre polynomials[24]:

$$P_{axis} = \sum_n c_n P_n(\cos\theta) \qquad (1)$$

with $c_n = \frac{(2n+1)}{2}\langle P_n(\cos\theta)\rangle$, where the brackets denote averaging and $\theta$ is the angle between the laser polarisation vector and the symmetry axis of the molecule. $\langle P_1(\cos\theta)\rangle$ is commonly called the orientation and $\langle P_2(\cos\theta)\rangle$ the alignment. The degree of alignment can be expressed as the expectation value $\langle P_2(\cos\theta)\rangle$ which ranges from 1 to -0.5. A positive value of the alignment indicates that the molecule is aligned parallel to the laser field and if it is negative, the molecule is aligned perpendicular to the laser field. $\langle P_2(\cos\theta)\rangle = 0$ means that there is no alignment, in this case $\langle\cos^2\theta\rangle = 1/3$. The advantage of using the Legendre polynomial $\langle P_2(\cos\theta)\rangle$ over $\langle\cos^2\theta\rangle$ is that the Legendre polynomials are orthogonal and $\cos^2(\theta)$ is not orthogonal to $\cos(\theta)$.

Sugita *et al.* studied the alignment of $CH_3I$ in a cold molecular beam with a nanosecond laser at 1064 nm.[14] They found an alignment for $CH_3I$ of $\langle P_2(\cos\theta)\rangle = 0.12$ ($\langle\cos^2\theta\rangle = 0.41$) at $1{\cdot}10^{11}$ W/cm$^2$ above which the alignment saturates. The estimated temperature of the molecular beam was 7 K. Adiabatic alignment of $CH_3I$ molecules induced by non resonant nanosec-

[a]Institute of Atomic and Molecular Physics, Jilin University, Changchun 130012, PR China, E-mail: dajund@jlu.edu.cn
[b]Jilin Provincial Key Laboratory of Applied Atomic and Molecular Spectroscopy, Jilin University, Changchun 130012, China
[c]Institute for Lasers, Life, and Biophotonics, Vrije Universiteit, de Boelelaan 1083, Amsterdam 1081 HV, The Netherlands

ond infrared laser pulses was studied using velocity map imaging by Trippel *et al.*[15] These authors found a saturation value of the alignment of $\langle P_2(\cos\theta)\rangle = 0.21$ ($\langle\cos^2\theta\rangle = 0.47$) at an intensity of $5{\cdot}10^{11}$ W/cm$^2$. The temperature of the molecular beam was estimated to be 12 K. In contrast to adiabatic alignment, impulsive (non adiabatic) alignment can induce laser field-free alignment of the molecular axis (revivals). Hamilton *et al.* employed 0.75 ps pulses to impulsively align $CH_3I$; the maximum alignment found was $\langle P_2(\cos\theta)\rangle = 0.24$ ($\langle\cos^2\theta\rangle = 0.49$) at $1.3{\cdot}10^{13}$ W/cm$^2$.[18] The different beam temperatures and consequently the different rotational states involved make it difficult to compare the results quantitatively. Rotational state selection makes it possible to study the alignment of only one rotational quantum state. In general symmetric, and nearly symmetric molecules, with a non zero dipole moment, can be selected in a specific rotational state by focusing through a hexapole. In practice polar symmetric top molecules with $|JKM\rangle$ eigenstates with the product of KM $< 0$ can be selected. The state-selected molecules can be oriented by relatively small electric fields and in our experimental geometry the molecules will be oriented anti-parallel to the direction of the weak extraction field.

In this paper the laser alignment of the $|1 \pm 1 \mp 1\rangle$ state of $CH_3I$ is studied, along with the effects it has on the dissociation dynamics of the molecule. At the extrema of the revival structure where the maxima in parallel and perpendicular alignment occur, velocity map images of the $I^+$ fragment from the $CH_3^+ + I^+$ CE channel are recorded. In the velocity map ion imaging configuration the electric extraction field is perpendicular to the laser polarisation vector. The hexapole state-selected molecules will be easily oriented along the extraction field which will make the distribution around the laser polarisation vector non-isotropic. Velocity map ion imaging projects the three dimensional ion distribution onto the two dimensional plane of the MCP detector. In most laser alignment studies the angular distribution of the projected $\theta_{2D}$ distribution is determined and the revival transient of $\cos\theta_{2D}$ and $\cos^2\theta_{2D}$ is compared with the calculated revival transient to derive the alignment parameters[25]. In this paper we will discuss a method to directly obtain the alignment parameters from the velocity map images. The inverse Abel transformation relates the projected $\theta_{2D}$ angular distributions to the three dimensional angular distributions which reflect the alignment parameters. However, this reconstruction method can only be applied to symmetric distributions around the laser polarisation. We will show that at high laser intensities this symmetry is sufficiently present. The recorded ion images are a product of the recoil dynamics of the fragmentation process and the alignment dynamics of the parent molecule. The decomposition process to obtain the alignment parameters from the experimental data directly will be discussed in detail.

## 2 Theory

The theory we derive here is a special case of the very general theory derived by Hamilton and Seideman *et al.*[18,26,27] In this paper we consider only the case where the laser field is perpendicular to the static field. The Hamiltonian consists of three parts:

$$H = H_{\rm rot} + H_{\rm Stark} + V(t) \tag{2}$$

where $H_{\rm Stark}$ and $V(t)$ represent the interaction with the static field and the time dependent laser field, respectively. The interaction of the molecular dipole ($\mu$) with a static electric field (E) is given by $H_{Stark} = \mu E \cos\theta_s$, where $\theta_s$ is the angle between the symmetry axis of the symmetric top molecule considered here, and the laboratory $Z$-axis, which is taken along **E**, and which acts as the quantization axis, see Fig. 1. The first step of the calculation is to diagonalise the Hamiltonian $H_{\rm rot} + H_{\rm Stark}$. The diagonalisation of the Hamiltonian is carried out using a standard algoritm.[28] The initial state is a pure rotational state but after interaction with the static electric field, this state is mixed with higher rotational states. However, for the weak extraction field used in our experiment the contribution of the higher rotational states is small. The interaction with the laser is described by:

$$V(t) = -\frac{1}{3}\Delta\alpha I_L(t)\cos^2(\theta_L) \tag{3}$$

with $\Delta\alpha = \alpha_{zz} - \alpha_{xx}$ (cm/W), where $\alpha_{zz}$ and $\alpha_{xx}$ are the components of the polarisability tensor parallel and perpendicular to the molecular symmetry axis, $I_L$ is the laser intensity (W/cm$^2$) and $\theta_L$ is the angle between the laser polarisation vector and the symmetry axis of the molecule.[18] The intensity of the laser $I_L(t)$ is related to the laser electric field by:

$$I_L(t) = \frac{c\varepsilon_0 n}{2}|E(t)|^2 \tag{4}$$

in which c is the speed of light, $\varepsilon_0$ the vacuum permittivity and n the refractive index. For a laser with a Gaussian temporal profile the time dependence of the electric field is given by:

$$E(t) = E_0 \exp(-2ln(2)(\frac{t}{\tau_p})^2) \tag{5}$$

with $\tau_p$ the laser pulse duration. The definition used in our simulation for the temporal dependence of the intensity profile of the laser is given by:

$$I_L(t) = \frac{c\varepsilon_0 n}{2}E_0^2 \exp(-4ln(2)(\frac{t}{\tau_p})^2) = I_0 \exp(-4ln(2)(\frac{t}{\tau_p})^2) \tag{6}$$

If the laser polarisation is perpendicular to the static field direction, $\cos\theta_L$ can be written as $\cos\theta_L = \sin\theta_s\cos\phi$, with $\phi$ the azimuthal angle in the space-fixed frame. We note that unlike Friedrich and Herschbach we do not take the laser polarisation as the quantization axis, since the molecules are state-selected by using a static hexapole field and after exiting the hexapole orient adiabatically along a guiding field or, in our case, the extraction field.[29] In terms of Wigner rotation matrices ($D^J_{MK}$), $\cos\theta_L$ can be written as[24]:

$$\cos\theta_L = \frac{1}{2}\sqrt{2}\left(D^1_{-10}(\phi,\theta_s,\chi) - D^1_{10}(\phi,\theta_s,\chi)\right) \tag{7}$$

where the Euler angles $\phi, \theta_s, \chi$, which will be omitted in the following, relate the laboratory fixed frame and the molecular

frame. The term $\cos^2\theta_L$ from Eq. 3 can be expressed as:

$$\cos^2\theta_L = \frac{1}{2}\left(D^1_{-10} - D^1_{10}\right)^2. \quad (8)$$

This can be written in terms of the Legendre polynomial $P_2(\cos\theta_L)$. The laser interaction induces an alignment distribution of the molecule along the laser polarisation axis, which can be written as a series expansion in Legendre polynomials. The alignment distribution in the laser frame is related to that in the static field frame by the spherical harmonic addition theorem[24]:

$$P_l(\cos\theta_L) = \frac{4\pi}{2l+1}\sum_m Y^*_{lm}(\theta_s,\phi_s)Y_{lm}(\theta,\phi) \quad (9)$$

where $\theta$ and $\phi$ are polar angles of the laser polarisation direction in the laboratory frame. If the laser polarisation is chosen perpendicular to the static field, $\theta = \pi/2$ and $\phi$ may be chosen to be zero. For the first four Legendre polynomials we find

$$P_1(\cos\theta_L) = \frac{1}{2}\sqrt{2}\left[(D^1_{-10} - D^1_{10})\right] \quad (10)$$

$$P_2(\cos\theta_L) = \frac{1}{2}\left[\sqrt{\frac{3}{2}}(D^2_{20}+D^2_{-20}) - D^2_{00}\right] \quad (11)$$

$$P_3(\cos\theta_L) = \frac{1}{2}\left[\frac{1}{2}\sqrt{5}(D^3_{-30} - D^3_{30}) + \frac{1}{2}\sqrt{3}(D^3_{10} - D^3_{-10})\right] \quad (12)$$

$$P_4(\cos\theta_L) = \frac{1}{8}\left[\frac{1}{2}\sqrt{70}(D^4_{40}+D^4_{-40}) - \sqrt{10}(D^4_{20}+D^4_{-20}) + 3D^4_{00}\right] \quad (13)$$

These equations are used to calculate the spatial distribution of the symmetry axis of the molecule which will be discussed in the next section. Writing $\cos^2\theta_L$ in Eq. 8 as $\frac{1}{3}(2P_2(\cos\theta_L)+1)$, and applying Eq. 11, the Hamiltonian for the molecular rotation in the presence of an electrostatic field with a laser field perpendicular to the static field can be written as

$$H = BJ(J+1) + (A-B)K^2 - \mu E_s D^1_{00} - \frac{1}{3}\Delta\alpha I_L\left[\sqrt{\frac{3}{2}}(D^2_{20}+D^2_{-20}) - \frac{1}{2}D^2_{00}\right] \quad (14)$$

where $E_s$ is the static electric field (e.g. extraction field) in (kV/cm). The orientation independent contribution to the polarisability term has been omitted. If the eigenfunctions of the Hamiltonian in Eq. 14 are written as linear combinations of the pure rotational functions $|JMK\rangle$, the elements corresponding to the laser interaction are:

$$\langle JMK| - \frac{1}{3}\Delta\alpha I_L\left[\sqrt{\frac{3}{2}}(D^2_{20}+D^2_{-20}) - \frac{1}{2}D^2_{00}\right]|J'M'K'\rangle \quad (15)$$

Writing the rotation wave functions as Wigner rotation matrices [24]:

$$|JMK\rangle = \sqrt{\frac{2J+1}{8\pi^2}}D^{J*}_{MK}(\phi,\theta,\chi) = (-1)^{M-K}\sqrt{\frac{2J+1}{8\pi^2}}D^J_{-M-K}(\phi,\theta,\chi) \quad (16)$$

The elements of the interaction Hamiltonian given in Eq. 15 take the form:

$$-\sqrt{\frac{1}{24}}\left[\begin{pmatrix} J & 2 & J' \\ M & 2 & -M-2\end{pmatrix} + \begin{pmatrix} J & 2 & J' \\ M & -2 & -M+2\end{pmatrix} - \sqrt{\frac{2}{3}}\begin{pmatrix} J & 2 & J' \\ M & 0 & -M\end{pmatrix}\right]\begin{pmatrix} J & 2 & J' \\ K & 0 & -K\end{pmatrix} \quad (17)$$

This equation needs to be multiplied by the factor $\sqrt{(2J+1)(2J'+1)}\Delta\alpha I_L$. The factor $(-1)^{K-M}$ is omitted since it is canceled by the factors $(-1)^{J-M}$ and $(-1)^{J-K}$ in the algebraic expressions of the Wigner 3−j−symbols. M′ may be different from M, but as a consequence of Eq. 14, even and odd M levels do not mix, so that no sign change due to these factors occur. Non-mixing of even and odd M-levels also leads to zero expectation values for $P_1(\cos\theta_L)$ and $P_3(\cos\theta_L)$, see Eq. 10 and Eq. 12. Now that we have established the Hamiltonian to describe the interaction with the static electric field and the laser electric field, we will closely follow the derivation of Hamilton *et al.* to obtain the equations for the rotational wave packet motion and only a brief description will be given here.[18] The time dependent wave functions can be expanded like:

$$|\psi(t)\rangle = \sum_{J,M} c_{JM}(t)exp(-iE_{rot+Stark}t/\hbar)|JMK\rangle \quad (18)$$

The initial coefficients are determined by the outcome of the diagonalisation of the Hamiltonian $H_{\rm rot} + H_{\rm Stark}$. Only during the laser pulse do the complex coefficients $c_{JM}$ become time dependent and employing the time dependent Schrödinger equation yields:

$$i\frac{\partial}{\partial t}c_{J'M'}(t) = \sum_{J,M}\langle J'M'|V(t)|JM\rangle c_J(t)e^{i\omega_{mn}t} \quad (19)$$

These coupled equations are integrated with a fourth order Runge-Kutta routine.[28] The equation describing the time dependence of the alignment terms is given by:

$$\langle P_l(\cos\theta_L)\rangle(t) = \sum_{J,J'M,M'} c_{JM}(t)c^*_{J'M'}(t)\langle JMK|P_l(\cos\theta_L)|J'M'K'\rangle \exp\left(-i(E_{JMK} - E_{J'M'K'})t/\hbar\right) \quad (20)$$

Eq's. 10 to 13 combined with Eq. 16 are used to express the matrix elements in the right hand side of the equation into Wigner 3−j−symbols. The sums over the Wigner 3−j−symbols are efficiently evaluated using the recursive algorithms described by Schulten and Gordon.[30]

## 3 Experimental

The femtosecond laser used is the Libra (Coherent) an all-in-one ultrafast oscillator and regenerative amplifier laser system operating at a 1 kHz repetition rate. Typically, the pulses have a duration of 100 fs (FWHM) and an energy of 4 mJ. The laser pulses are split into two beams which serve as an alignment and probe laser. The alignment laser pulse is stretched to about 300 fs using

70 mm BK7 glass. The polarisation of both the alignment and the probe laser are parallel to the imaging plane and both laser beams are focused into the detection chamber using a 25 cm focal length lens. Fig. 1 shows the experimental setup. The molecular

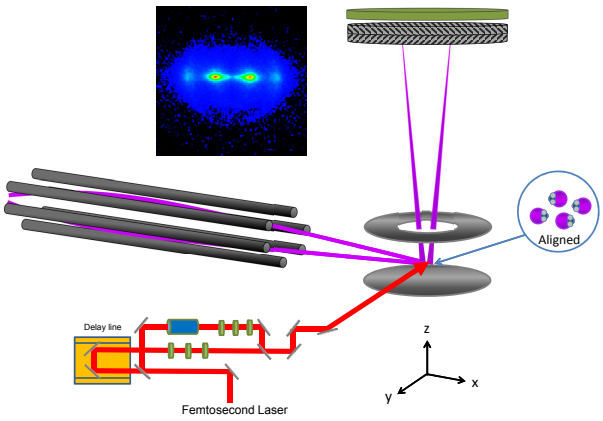


**Fig. 1** Schematic view of the experimental setup, for details see the text. The electric field is along the Z-axis and the laser polarisation is along the X-axis. A velocity map ion image of the $I^+$ ion is shown recorded at the peak at the half revival time.

beam machine consists of three chambers, a source chamber, a chamber with the hexapole and the chamber containing the ion optics and the detector. A supersonic molecular beam of 2.5% $CH_3I$ seeded in Neon is produced at a 1.5 bar stagnation pressure through a 0.5 mm orifice of a pulsed valve (General Valve Series 9) at a repetition rate of 10 Hz. The molecular beam passes through a skimmer (Beam Dynamics, diameter 2 mm) positioned about 3 cm behind the nozzle, that separates the source chamber from the hexapole chamber. The entrance of the hexapole is 30 cm from the nozzle. The hexapole has a length of 100 cm and an inner diameter of 8 mm. The Time of Flight (TOF) tube and the imaging detector are mounted perpendicular to the velocity vector of the molecular beam. Halfway between the repeller and extractor plates (separated by 15 mm), the molecular beam is crossed at right angles with the laser beams. The total distance from the nozzle to the laser interaction region is 158 cm. The ions produced in the interaction region are accelerated into a 50 cm long TOF tube. The extraction field used is 300 V/cm. The imaging detector is equipped with a chevron dual MCP (Tectra) (d =87 mm active diameter) coupled to a fast phosphor screen (P47). The MCPs are gated by applying a fast rising voltage pulse of 500 ns width (DEI, PVX−4130, ±6 KV pulse generator). The electrons ejected from the back side of the MCP are accelerated towards the fast phosphor screen (P47). The light from the phosphor is imaged by a camera lens on a CCD camera (IDS Imaging UI−2230SE−M−GL Rev.3). At the same time part of the light is detected by a photomultiplier (Zolix Instruments Co. Ltd.) to monitor the total TOF ion signal. The repeller-extractor region is configured for velocity map imaging[31]. For the Abel inversion the BASEX algorithm has been employed[32]. To quantify the alignment dynamics we measured the total ion yield of $CH_3I^+$, $I^+$ and $I^{2+}$ in the range 1 - 80 ps from methyliodide seeded in Neon. The hexapole gives an amplification of about 4 times for the $CH_3I^+$ ion yield which indicates that the molecular beam consist for about 75 % of $CH_3I$ in the $|JMK\rangle = |1 \pm 1 \mp 1\rangle$ state. The intensity of the alignment laser was chosen such that this laser alone did not produce any (fragment) ions. We have determined the peak intensity of the alignment laser by measuring the ionisation rate of Xenon as a function of laser energy, from which we estimated $I_0$ to be about $5{\cdot}10^{13}$ W/cm$^2$.[33] Cross correlation of the alignment and the probe laser shows that the pulse duration of the alignment laser is around 275 fs.

## 4 Results and Discussion

Fig. 2 shows the calculated spatial distribution of the molecular axis parallel and perpendicular to the extraction field. The horizontal axis of the figure gives the time between the alignment laser pulse and the probe laser pulse. The extraction field is in the direction of the Time-Of-Flight detector and the laser polarisation vector is in the plane of the MCP, perpendicular to the Time-Of-Flight detector. The inverse Abel transformation is crucial for the

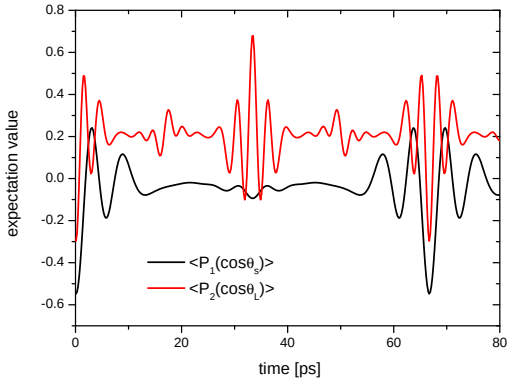


**Fig. 2** The calculated transients of $\langle P_1(\cos\theta_s)\rangle$ (black) and $\langle P_2(\cos\theta_L)\rangle$ (red) are the dominant contributions to the orientation distribution around, respectively, the direction of the extraction field (Z-axis), and the laser polarisation vector (X-axis), see Fig. 1

data analysis in photo-fragment-ion imaging and photo-electron imaging. The inverse Abel transformation relates the Abel projected $\theta_{2D}$ radial and angular density distributions to the radial and angular density distributions in 3D space which reflect the alignment parameters. However, this reconstruction method can only be applied to cylindrically symmetric distributions around the laser polarisation. The angular distribution of the molecular axis around the Z-axis is given by Eq. 1. After application of the alignment pulse a wavepacket is created which leads to alignment of the molecular axis along the laser polarisation-axis, X, but which does not necessary lead to a zero orientation along the Z-axis. If $\langle P_1(\cos\theta_s)\rangle$ is non-zero, the distribution along the X-axis will contain contributions such as $\langle D^1_{10}(\theta_L,\phi_L,0)\rangle$, with polar angle $\theta_L$ and azimuthal angle $\phi_L$ and hence will no longer be axially

symmetric. As is shown in Fig. 2, the $P_1(\cos\theta_s)$ term is small around the half revival time. Also at the maxima of $\langle P_2(\cos\theta_L)\rangle$ (red curve) at the full revival time the $P_1(\cos\theta_s)$ term is very close to zero. Only at the minimum at the full revival time is the axial symmetry broken.

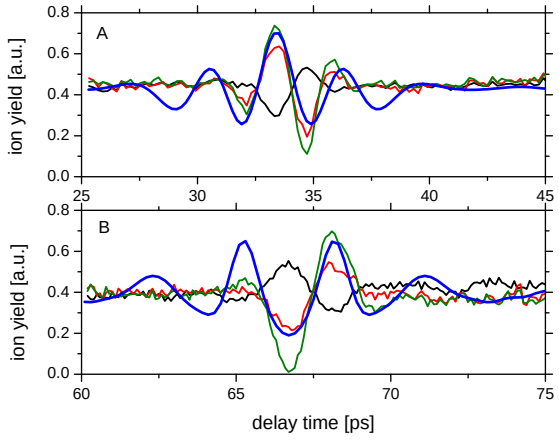


**Fig. 3** Experimentally observed ion signals around the half revival time (top panel) and full revival time (bottom panel) compared with the calculation. The black line represents the $CH_3I^+$ signal, the red line the $I^+$ signal and the olive line the $I^{2+}$ signal, respectively. The calculated ion signal (blue line) shows the calculated transient for the experimentally determined pulse duration of 275 fs and laser intensity $I_0$ of $5{\cdot}10^{13}$ W/cm$^2$.

In Fig. 3 the yields of three different ion species are plotted as a function of delay time between the alignment and the probe laser, both polarised along the X-axis. The solid blue line is the calculated ion signal which shows the scaled ion yield $I = \sigma(\theta_L)[c_0 + c_2P_2(\cos\theta_L) + c_4P_4(\cos\theta_L) + c_6P_6(\cos\theta_L)]$, in which $\sigma(\theta_L)$ is the ionisation cross-section ($CH_3I^+$) or dissociation cross-section ($I^+$ or $I^{2+}$), respectively. This cross section is taken to be independent of $\theta_L$ and is used as a scaling factor between the calculated and experimentally determined ion signal. The calculated transient was obtained by employing a laser intensity of $5{\cdot}10^{13}$ W/cm$^2$ and a laser pulse duration of 275 fs. The only free parameter in the calculation is the scaling factor $\sigma(\theta_L)$. Fig. 3A shows the ion signal around the half revival time and Fig. 3B shows the ion signal around the full revival time. The figures show that the yield of the ionic fragments $I^+$ and $I^{2+}$ increases when the parent molecule is aligned along the laser polarisation and that it decreases when the parent molecule is aligned perpendicular to the laser polarisation. For the ionisation rate of the parent molecule the opposite behavior is observed. The orientation dependent ionization yield of several poly atomic molecules has been studied before[34,35]. The decrease in ionization yield of the parent $CH_3I^+$ ion can be explained by the fact that the electron which is removed is the non-bonding 5p$\pi$ electron. This non-bonding $\pi$ orbital is aligned perpendicular to the symmetry axis of the parent molecule. In the case that the parent molecule is aligned along the laser polarization vector the electron orbital is aligned perpendicular to the laser polarization vector giving rise to a decrease in the signal. The period of the oscillation of the calculated transient depends critically on the pulse duration as well as the intensity of the alignment laser. In this calculation we have used a polarisability $\Delta\alpha = 6$ Å$^3$ ($=1.0{\cdot}10^{-11}$ cm/W).[36] No quantitative agreement is obtained because the angular dependence of the ionisation and dissociation cross-section is not included in the calculation of the ion signal.

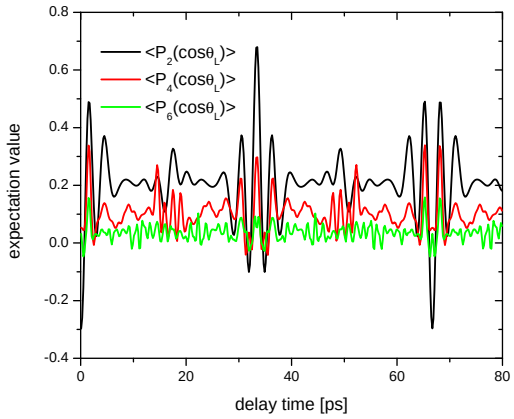


**Fig. 4** This Figure shows the calculated revival transients for $\langle P_2(\cos\theta_L)\rangle$ (black line), $\langle P_4(\cos\theta_L)\rangle$ (red line) and $\langle P_6(\cos\theta_L)\rangle$ (green line).

Fig. 4 shows the revival structure for the $P_2(\cos\theta_L)$, $P_4(\cos\theta_L)$ and $P_6(\cos\theta_L)$ alignment terms. The expectation value of the alignment parameter $P_n(\cos\theta_L)$ is plotted against the delay time between alignment and probe laser in picoseconds. Two distinct features can be observed, around about 32 ps, the half revival time (T/2) and around about 64 ps, the full revival time (T). Velocity map ion images are recorded at delay times where the revival transient exhibits minima and maxima of the $\langle P_2(\cos\theta_L)\rangle$ parameter. The angular distribution of these velocity map ion images are a product of the spatial distribution of the molecular axis of the parent molecule and the recoil dynamics, see Eq. 22. A general method to determine the laser induced molecular axis alignment for poly atomic molecules was published by Mikosch *et al*[37]. For state-selected symmetric top molecules a simpler method can be employed which will be described below.

**Table 1** Experimental angular distributions on different delay times in the revival

| delay time | $b_2/b_0$ | $b_4/b_0$ | $b_6/b_0$ |
|---|---|---|---|
| baseline | 2.88 | 2.49 | 1.51 |
| T/2 min | 1.55 | 0.69 | 0.39 |
| T/2 max | 4.21 | 5.17 | 4.98 |
| T min | 1.23 | 1.10 | 0.83 |
| T max | 3.87 | 5.08 | 5.88 |

If non-axially symmetric contributions to the angular distribution may be neglected, the distribution of the molecular symmetry axis along the laser polarisation axis, can be described by even

Legendre polynomials only[38]:

$$P_{axis} = c_0 + c_2 P_2(\cos\theta_L) + c_4 P_4(\cos\theta_L) + c_6 P_6(\cos\theta_L) \quad (21)$$

in which $c_n = \frac{2n+1}{2}\langle P_n(\cos\theta_L)\rangle$. The product of the alignment distribution with the recoil distribution is given by:

$$I(\theta_L) = P_{axis}\left[1 + \beta P_2(\cos\theta_L) + \gamma P_4(\cos\theta_L) + \delta P_6(\cos\theta_L)\right] \quad (22)$$

with $\beta, \gamma, \delta$ the asymmetry parameters of the recoil distribution. [24] The cross terms in the expansion are reducible and can be expanded in Legendre polynomials, for example:

$$P_2(\cos\theta_L)P_2(\cos\theta_L) = \frac{18}{35}P_4(\cos\theta_L) + \frac{2}{7}P_2(\cos\theta_L) + \frac{1}{5} \quad (23)$$

To compare the alignment and recoil parameters with the experimental angular distributions from the velocity map images we rewrite Eq. 22 as:

$$I(\theta_L) = [1 + \frac{b_2}{b_0}P_2(\cos\theta_L) + \frac{b_4}{b_0}P_4(\cos\theta_L) + \frac{b_6}{b_0}P_6(\cos\theta_L)] \quad (24)$$

the coefficients in front of the Legendre moments are combinations of the molecular axis alignment moments $c_n$ and the recoil parameters of the photo dissociation process given by:

$$b_0 = c_0 + \frac{1}{5}c_2\beta + \frac{1}{9}c_4\gamma + \frac{1}{13}c_6\delta \quad (25)$$

$$b_2 = c_2 + c_0\beta + \frac{2}{7}c_2\beta + \frac{2}{7}c_2\gamma + \frac{2}{7}c_4\beta + \frac{100}{693}c_4\gamma + \frac{25}{143}c_4\delta + \frac{25}{143}c_6\gamma + \frac{14}{143}c_6\delta \quad (26)$$

$$b_4 = c_4 + c_0\gamma + \frac{18}{35}c_2\beta + \frac{20}{77}c_2\gamma + \frac{20}{77}c_4\beta + \frac{162}{1001}c_4\gamma + \frac{45}{143}c_2\delta + \frac{20}{143}c_4\delta + \frac{45}{143}c_6\beta + \frac{20}{143}c_6\gamma + \frac{252}{2431}c_6\delta \quad (27)$$

$$b_6 = c_6 + c_0\delta + \frac{5}{11}c_2\gamma + \frac{5}{11}c_4\beta + \frac{20}{99}c_4\gamma + \frac{14}{55}c_6\beta + \frac{28}{187}c_6\gamma + \frac{400}{3553}c_6\delta \quad (28)$$

The normalization condition dictates that $c_0$ = 1/2, see Eq. 21. Velocity map ion images for the $I^+$ fragment are recorded at different times for the rotational wavepacket from which the three asymmetry parameters $b_2/b_0$, $b_4/b_0$ and $b_6/b_0$ are determined, see Table 1. The calculations show that the base lines of the terms $\langle P_n(\cos\theta)\rangle$ are not zero, see Fig. 4. To decompose the alignment and recoil contributions to the angular distribution we need to define a base level, which we recorded at several delay times in between the revival structures. At delay times in between the two revival structures we find on average $b_2/b_0$ = 2.88, $b_4/b_0$ = 2.49, $b_6/b_0$ = 1.51, see Eq. 24. This angular distribution is indicated with baseline in Table 1. From the velocity map ion images recorded at the maximum and minimum in the observed alignment the alignment parameters $c_2$, $c_4$ and $c_6$ can be derived employing Eqns 25 - 28. The alignment parameters in between the revival structures are not zero and by integrating the revivals over time we find the average values $\langle P_2(\cos\theta_L)\rangle$ = 0.2 , $\langle P_4(\cos\theta_L)\rangle$ = 0.1 and $\langle P_6(\cos\theta_L)\rangle$ = 0.05, see Figure 4, which is used to estimate the base line alignment. We find for the recoil anisotropy parameters $\beta$ = 1.77, $\gamma$ = 0.50 and $\delta$ = -0.53. The recoil anisotropy parameters are related to the recoil distribution function of the $I^+$ fragment in the molecular frame and describe the Coulomb explosion process. [24] These recoil parameters are used to decompose the anisotropy parameters at the other delay times in the revival transient, see Table 2. The first line in Table 2 gives the value of the calculation and the second line the experimentally obtained value, for each indicated delay time. In the decomposition of the alignment and recoil parameters we have used the calculated values for the offset of the baseline. To ensure convergence the contribution of $c_n$ to the $b_n$ parameter must decrease with increasing n, which is indeed the case. Consider the last line from Table 2 for these experimental numbers the contribution of $c_2$ to $b_2$ is 52%, of $c_4$ 28% and $c_6$ 20%. The experimental error in the derived alignment parameters $C_2$, $C_4$ and $C_6$ is estimated to be about respectively 10%, 15% and 20%. However, in this error analysis the error in the cut-off in the $C_n$ expansion is not included which is small for $C_2$ but expected to be big for the $C_6$ coefficient.

**Table 2** Alignment parameters on different delay times in the revival

| delay time | | $\langle P_2(\cos\theta_L)\rangle$ | $\langle P_4(\cos\theta_L)\rangle$ | $\langle P_6(\cos\theta_L)\rangle$ |
|---|---|---|---|---|
| T/2 min | calc | -0.10 | 0.10 | -0.02 |
| T/2 min | exp | -0.05 | 0.00 | 0.05 |
| T/2 max | calc | 0.70 | 0.30 | 0.05 |
| T/2 max | exp | 0.69 | 0.36 | 0.40 |
| T min | calc | -0.30 | 0.05 | 0.02 |
| T min | exp | -0.12 | 0.04 | 0.05 |
| T max | calc | 0.50 | 0.28 | 0.15 |
| T max | exp | 0.40 | 0.22 | 0.41 |

We see that our simulations are in good agreement with the experimentally observed alignment parameters. Hamilton *et al.* employed 0.75 ps pulses to impulsively align $CH_3I$. The maximum alignment found was $\langle P_2(\cos\theta)\rangle$ = 0.24 ($\langle\cos^2\theta\rangle$ = 0.49) at $1.3{\cdot}10^{13}$ W/cm$^2$ using a cold molecular beam [18]. The maximum anti-alignment was found to be about $\langle P_2(\cos\theta)\rangle$ = -0.07. Hexapole state selection indeed gives an increase in the maximum obtainable alignment of the molecular axis. The maximum alignment we found is $\langle P_2(\cos\theta)\rangle$ = 0.69 and the maximum anti-alignment is $\langle P_2(\cos\theta)\rangle$ = -0.12.

Fig. 5 shows the calculated revival in the case of the perpendicular geometry (black line), the alignment and probe laser polarisation perpendicular to the extraction field, and the parallel geometry (red line) the alignment and probe laser polarisation parallel to the extraction field. The second case is normally used to calculate the revival structure although the experimental geometry is perpendicular and indeed the two revival transients look almost identical. Only at the quarter revival time T/4 (17 ps) and the three quarter revival time 3T/4 (50 ps) a small difference can be observed between the two calculated transients. However, our experimental signal to noise ratio is not sufficient to resolve these structures.

The numerical value of the $\langle P_2(\cos\theta)\rangle$ alignment term is in agreement with the simulations of Rouzee *et al.* who found a max-

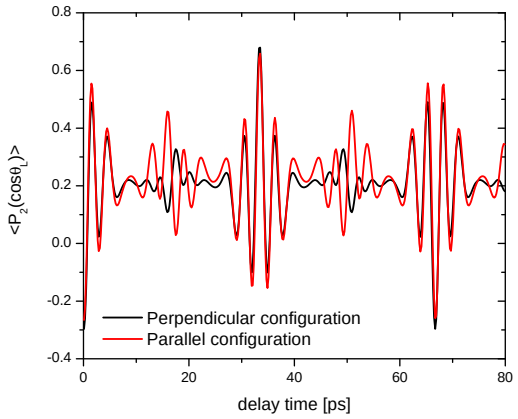


**Fig. 5** This Figure shows the simulated revival transients for $\langle P_2(\cos\theta)\rangle$ (black line) in the perpendicular geometry and $\langle P_2(\cos\theta)\rangle$ (red line) in the parallel geometry.

imum $\langle P_2(\cos\theta)\rangle = 0.6$ for hexapole state-selected $CH_3I$ at a laser intensity of $8.0{\cdot}10^{12}$ W/cm$^2$ in the absence of an electric field.[39] Note that Rouzee *et al.* take the laser polarisation vector to be the quantisation axis. The revival structure at T/4 and 3T/4 displays an opposite phase for the parallel and perpendicular geometry. Fleischer *et al.* attributed this phase shift to the contributions of even and odd J levels.[40] An detailed analysis of the difference is complicated because in the perpendicular geometry many more states are involved than in the parallel one. In the parallel geometry only mixing between different J-states occurs, whereas in the perpendicular also M states can mix, though only if they differ by an even number.

## 5 Conclusions

In this article we have given the theoretical relations to calculate the revival structure of $CH_3I$ in the $|JMK\rangle = |1 \pm 1 \mp 1\rangle$ state in a geometry in which the laser field is perpendicular to the static electric field. The period of the revivals in the ion signal is reproduced by the calculation without fitting any parameter except for an amplitude scaling factor. It is shown that with the experimentally favourable perpendicular geometry of the time-of-flight setup, concomitant deviations from the axial symmetry are sufficiently small to be neglected. The calculated alignment parameters $\langle P_n(\cos\theta_L)\rangle$, with n even, at the maximum alignment and anti-alignment correspond well with the values derived from the velocity map images. Hexapole state selection can increase the maximum observed alignment $\langle P_2(\cos\theta_L)\rangle$ to 0.7.

## 6 Acknowledgments

WGR and DD are supported by CNSF under Grant no's: 11304117, 11374122, 91221301 and 1127403. WGR acknowledges many helpful discussions with dr. A. Gijsbertsen.

## References

1 P. R. Brooks, *Science*, 1976, **193**, 11 – 16.
2 D. H. Parker and R. B. Bernstein, *Annu. Rev. Phys. Chem.*, 1989, **40**, 561 – 595.
3 T. P. Rakitzis, A. J. van den Brom and M. H. M. Janssen, *Science*, 2004, **303**, 1852 – 1854.
4 M. Nakamura, D.-C. Che, P.-Y. Tsai, K.-C. Lin and T. Kasai, *J. Phys. Chem. A*, 2013, **117**, 8157 – 8162.
5 X. Xie, K. Doblhoff-Dier, S. R. H. Xu, M. Schöffler, D. Kartashov, S. Erattupuzha, T. Rathje, G. Paulus, K. Yamanouchi, A. Baltuška, S. Gräfe and M. Kitzler, *Phys. Rev. Lett.*, 2014, **112**, 163003.
6 V. Aquilanti, M. Bartolomei, F. Pirani, D. Cappelletti, F. Vecchiocattivi, Y. Shimizu and T. Kasai, *Phys. Chem. Chem. Phys*, 2005, **7**, 291 – 300.
7 M. Busuladzić, A. Gazibegović-Busuladzić, D. B. Milosević and W. Becker, *Phys. Rev. Lett*, 2008, **100**, 203003.
8 M. Okunishi, R. Itaya, K. Shimada, G. Prümper, K. Ueda, M. Busuladžić, A. Gazibegović-Busuladžić, D. B. Milošević and W. Becker, *Phys. Rev. Lett.*, 2009, **103**, 043001.
9 T. Kanai, S. Minemoto and H. Sakai, *Nature*, 2005, **435**, 470 – 474.
10 Y. Mairesse, J. Higuet, N. Dudovich, D. Shafir, B. Fabre, E. Mevel, E. Constant, S. Patchkovskii, Z. Walters, M. Ivanov and O. Smirnova, *Phys. Rev. Lett*, 2010, **104**, 213601.
11 J. Itatani, J. Levesque, D. Zeidler, H. Niikura, H. Pépin, J. Kieffer, P. B. Corkum and D. M. Villeneuve, *Nature*, 2004, **432**, 867 – 871.
12 C. Vozzi, M. Negro, F. Calegari, G. Sansone, M. Nisoli, S. D. Silvestri and S. Stagira, *Nat. Phys.*, 2011, **7**, 822 – 826.
13 J. J. Larsen, H. Sakai, C. P. Safvan, I. Wendt-Larsen and H. Stapelfeldt, *J. Chem. Phys*, 1999, **111**, 7774 – 7781.
14 A. Sugita, M. Mashino, M. Kawasaki, Y. Matsumi, R. J. Gordon and R. Bersohn, *J. Chem. Phys.*, 2000, **112**, 2164 – 2167.
15 S. Trippel, M. Stei, C. Eichhorn, R. Otto, P. Hlavenka, M. Weidemüller and R. Wester, *J. Chem. Phys.*, 2011, **134**, 104306.
16 F. Rosca-Pruna and M. J. J. Vrakking, *Phys. Rev. Lett.*, 2001, **87**, 153902.
17 K. F. Lee, I. V. Litvinyuk, P. W. Dooley, M. Spanner, D. M. Villeneuve, and P. B. Corkum, *J. Phys. B. Mol. Opt. Phys*, 2004, **37**, L43 – L48.
18 E. Hamilton, T. Seideman, T. Ejdrup, M. D. Poulson, C. Z. Bisgaard, S. S. Viftrup and H. Stapelfeldt, *Phys. Rev. A*, 2005, **72**, 043402.
19 I. Znakovskaya, M. Spanner, S. De, H. Li, D. Ray, P. Corkum, I. V. Litvinyuk, C. L. Cocke and M. F. Kling, *Phys. Rev. Lett.*, 2014, **112**, 113005.
20 L. Holmegaard, J. H. Nielsen, I. Nevo and H. Stapelfeldt, *Phys. Rev. Lett.*, 2009, **102**, 023001.
21 F. Filsinger, J. Küpper, G. Meijer, L. Holmegaard, J. H. Nielsen, I. Nevo, J. L. Hansen and H. Stapelfeldt, *J. Chem. Phys.*, 2009, **131**, 064309.
22 J. H. Nielsen, P. Simesen, C. Z. Bisgaard, H. Stapelfeldt, F. Filsinger, B. Friedrich, G. Meijer and J. Küpper, *Phys. Chem. Chem. Phys.*, 2011, **13**, 18971 – 18975.
23 O. Ghafur, A. Rouzée, A. Gijsbertsen, W. K. Siu, S. Stolte and

M. J. J. Vrakking, *Nat. Phys*, 2009, **5**, 289 – 293.
24 *Angular Momentum*, ed. R. N. Zare, Wiley, New York, 1988.
25 S. Luo, R. Zhu, L. He, W. Hu, X. Li, P. Ma, C. Wang, F. Liu, W. G. Roeterdink, S. Stolte and D. Ding, *Phys. Rev. A*, 2015, **91**, 053408.
26 T. Seideman and E. Hamilton, *Advances in Atomic, Molecular and Optical Physics*, 2006, **52**, 289 – 329.
27 M. Artamonov and T. Seideman, *J. Chem. Phys.*, 2008, **128**, 154313.
28 *Numerical Recipes 2*, ed. W. H. Press, B. P. Flannery, S. A. Teukolsky and W. T. Vetterling, Cambridge University Press, New York, 1990.
29 B. Friedrich and D. Herschbach, *J. Chem. Phys*, 1999, **111**, 6157 – 6160.
30 K. Schulten and R. G. Gordon, *Comp. Phys. Comm.*, 1976, **11**, 269 – 278.
31 A. T. J. B. Eppink and D. H. Parker, *Rev. Sci. Instrum*, 1997, **68**, 3477 – 3484.
32 V. Dribinski, A. Ossadtchi, V. A. Mandelshtam and H. Reisler, *Rev. Sci. Instrum*, 2002, **73**, 2634 – 2642.
33 S. M. Hankin, D. M. Villeneuve, P. B. Corkum and D. M. Rayner, *Phys. Rev. A*, 2001, **64**, 013405.
34 J. Mikosch, A. E. Boguslavskiy, I. Wilkinson, M. Spanner, S. Patchkovskii and A. Stolow, *Phys. Rev. Lett.*, 2013, **110**, 023004.
35 J. Hansen, L. Holmegaard, J. H. Nielsen, H. Stapelfeldt, D. Dimitrovski and L. B. Madsen, *J. Phys. B: At. Mol. Opt. Phys.*, 2012, **45**, 015101.
36 P. T. van Duijnen and M. Swarth, *J. Phys. Chem. A*, 1998, **102**, 2399 – 2407.
37 J. Mikosch, C. Bisgaard, A. Boguslavskiy, I. Wilkinson and A. Stolow, *J. Chem. Phys.*, 2013, **139**, 024304.
38 M. H. M. Janssen, J. W. G. Mastenbroek and S. Stolte, *J. Phys. Chem. A*, 1997, **101**, 7605 – 7613.
39 A. Rouzée, A. Gijsbertsen and M. J. J. Vrakking, *Progress in Ultrafast Intense Laser Science, Springer Series in Chemical Physics*, 2010, **99**, 45 – 73.
40 S. Fleischer, Y. Khodorkovsky, E. Gershnabel, Y. Prior and I. S. Averbukh, *Isr. J. Chem*, 2012, **52**, 414 – 437.